THE JOURNAL OF PHYSICAL CHEMISTRY LETTERS
A JOURNAL OF THE AMERICAN CHEMICAL SOCIETY

pubs.acs.org/JPCL

Letter

# Evolution of Structure and Optoelectronic Properties During Halide Perovskite Vapor Deposition

Vladimir Held, Nada Mrkyvkova,* Peter Nádaždy, Karol Vegso, Aleš Vlk, Martin Ledinský, Matej Jergel, Andrei Chumakov, Stephan V. Roth, Frank Schreiber, and Peter Siffalovic

Cite This: *J. Phys. Chem. Lett.* 2022, 13, 11905−11912

Read Online

ACCESS | Metrics & More | Article Recommendations | Supporting Information

**ABSTRACT:** The efficiency of perovskite-based solar cells has increased dramatically over the past decade to as high as 25%, making them very attractive for commercial use. Vapor deposition is a promising technique that potentially enables fabrication of perovskite solar cells on large areas. However, to implement a large-scale deposition method, understanding and controlling the specific growth mechanisms are essential for the reproducible fabrication of high-quality layers. Here, we study the structural and optoelectronic kinetics of $MAPbI_3$, employing *in-situ* photoluminescence (PL) spectroscopy and grazing-incidence small/wide-angle X-ray scattering (GI-SAXS/WAXS) simultaneously during perovskite vapor deposition. Such a unique combination of techniques reveals $MAPbI_3$ formation from the early stages and uncovers the morphology, crystallographic structure, and defect density evolution. Furthermore, we show that the nonmonotonous character of PL intensity contrasts with the increasing volume of the perovskite phase during the growth, although bringing valuable information about the presence of defect states.

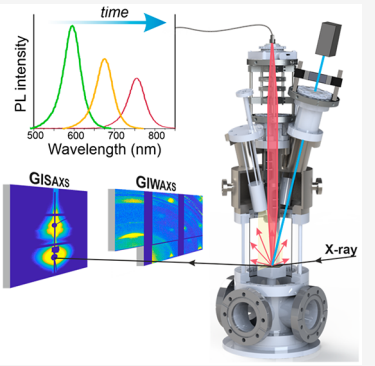


The increasing demand for electric energy requires more efficient and cost-effective technologies that are less technically challenging. Here, solar cells based on organic lead halide perovskites have shown great potential as an emerging photovoltaic technology.[1−4] This relatively new material, possessing high absorption, tunable direct bandgap, and extensive compositional engineering possibilities, has made remarkable progress with ever-increasing power conversion efficiency (PCEs) exceeding 25%.[5−8] As apparent by their notation, the organic lead halide perovskite films are formed by a chemical reaction between at least two precursors—lead halide, such as $PbI_2$ or $PbCl_2$, and organic halide, e.g., $CH_3NH_3I$, $CH_3NH_3Cl$, or $CH_5IN_2$ (MAI, MACl or FAI, respectively). Numerous fabrication methods have been developed to prepare perovskite layers, with the solution-processed spin coating being the most commonly used. Although the spin coating is advantageous for basic laboratory research due to its rapid manufacturing processes and low equipment costs, it is not suitable for large-scale industrial/commercial production.[9−12] One of the reasons for this is a high material waste rate of over 90%.[13] Furthermore, poor control of crystallinity and stoichiometry occurs in the case of the incomplete reaction of precursors during annealing, leading to poor batch-to-batch reproducibility.[14]

The vapor-based deposition technique, where the solid precursors are thermally evaporated onto the substrate in a high vacuum, provides several advantages over wet processes.[15] This technique allows the fabrication of high-purity layers, where the film thickness can be precisely controlled on a large scale. Moreover, in view of the recent advances in high-efficiency perovskite/silicon tandem solar cells,[16,17] it provides a tool for precise codeposition of multiple layers without affecting the underlying substrate. Thus, vapor deposition is a perspective method, especially for multijunction or all-perovskite tandem solar cells.[18,19]

Since vapor deposition, requiring dedicated/specialized high-vacuum deposition chambers, is not an extensively utilized technique for perovskite fabrication, the majority of published work is focused on the specific deposition parameters and their influence on the perovskite layer quality.[11,12,20−22] The main cause is the nontrivial evaporation of the organic precursor, typically MAI, that has a low sticking coefficient influencing its adsorption onto the substrate.[20,21] However, to the best of our knowledge, a comprehensive understanding of the perovskite evolution during vapor deposition in terms of morphology and electronic and structural properties is missing. To obtain an unbiased picture during perovskite formation, noninvasive *in-situ* experimental techniques need to be employed. Interrupting growth to perform various *ex situ* measurements under ambient conditions can result in misleading data, as perovskites are sensitive to humidity and light exposure.[23]

**Received:** November 10, 2022
**Accepted:** December 13, 2022
**Published:** December 16, 2022






https://doi.org/10.1021/acs.jpclett.2c03422
*J. Phys. Chem. Lett.* 2022, 13, 11905−11912

Here we present a simultaneous measurement of *in-situ* photoluminescence (PL) and grazing-incidence small/wide-angle X-ray scattering (GI-SAXS/WAXS) that reveals the electronic and structural changes during vapor-based growth of the archetypal $MAPbI_3$ perovskite. Such a unique combination of measuring techniques enables observation of perovskite phase formation from early stages and reveals the time evolution of defect density, morphology, and crystallographic structure. We show that perovskite formation is similar to wet deposition despite a different growth method. Specifically, the overall PL intensity is not directly proportional to the perovskite volume phase. The nonmonotonous character of PL was observed during growth, indicating the formation of defect states at the grain boundaries. We believe that the combined PL and GI-SAXS/WAXS techniques presented here are of fundamental importance for applying advanced passivation techniques that would lead to efficient perovskite layers beneficial for various optoelectronic applications.

We performed a vapor deposition of $MAPbI_3$ perovskite, where $PbI_2$ and MAI precursors were evaporated from the crucibles onto an unheated Si substrate (with native oxide) in a vacuum chamber with a base pressure of $\sim 10^{-6}$ mbar. Once the precursors' temperature was stabilized, the shutters on both crucibles were opened simultaneously, and the perovskite layer started to form. The *in-situ* PL and GI-SAXS/WAXS were measured simultaneously during the $MAPbI_3$ formation, as schematically outlined in Figure 1. A detailed description of the experimental conditions and setup can be found in Supporting Information and ref 24.

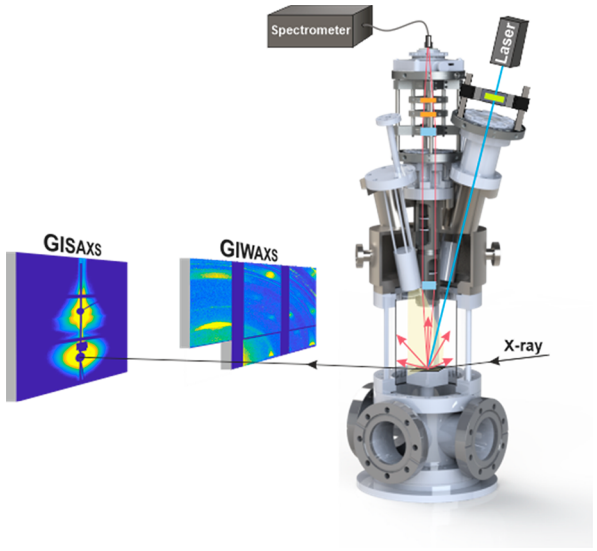


**Figure 1.** Schematic drawing of the deposition chamber and the scattering geometry.

To thoroughly understand the processes during perovskite growth, the surface morphology needs to be investigated with a temporal resolution faster than the progressing structural changes. Interrupting the perovskite deposition to acquire real-space images at different growth stages could be problematic, since it typically requires exposing the perovskite layers to ambient conditions. Perovskites are very sensitive to air or/and humidity,[1,23,25,26] so we used *in-situ* GISAXS to monitor the surface morphology noninvasively during the layer formation.

Figure 2a shows the GISAXS diffraction pattern measured ~2 min after opening the shutters on $PbI_2$ and MAI. Here, diffuse out-of-plane scattering can be observed (indicated by magenta dashed lines in Figure 2a), containing information about the perovskite layer morphology. The diffuse scattering rods along $q_\perp$ indicate laterally ordered nanostructures at the beginning of perovskite growth. We confirmed the existence of such perovskite nanostructures at the beginning of perovskite deposition by taking postgrowth AFM images (see Figure 2b). The AFM scans were done on a perovskite layer where the growth was interrupted ~2 min after the deposition started. The AFM image shows isolated perovskite islands with an average particle size distribution $d_{AFM} = (90 \pm 10)$ nm and an average height of ~5.5 nm. The mean interisland spacing was determined by calculating the radial power spectral density function (PSDF) and fitting it subsequently by a Gauss function (see Figure 2c). The maximum of the fit is at ~0.023 $nm^{-1}$, corresponding to the mean distance between islands $D_{AFM} \approx 275$ nm. We note that more AFM scans, including for thicker $MAPbI_3$ layers, are shown in Figure S1.

Similarly, the mean distance between the islands can be deduced from the lateral patterns in the GISAXS scans. The reciprocal distance $2\Delta q_{||}$ between the out-of-plane peaks (shown in Figure 2a) gives the average correlation distance between the perovskite islands $D \approx 2\pi/\Delta q_{||}$.[27,28] The time evolution of the out-of-plane scattering peaks, obtained by integrating the reciprocal area in the vicinity of $q_\perp \approx 0.09$ $Å^{-1}$, is shown in Figure 2d. At the beginning of the deposition, the peak position is at $q_{||} \approx \pm 0.017$ $nm^{-1}$ and continuously shifts toward lower values as the perovskite growth proceeds. Such evolution of roughness spatial frequencies (represented in this case by the position of the out-of-plane peaks along $q_{||}$) from larger values toward lower ones is typical for mounded surfaces during vapor deposition.[29] With increasing deposition time, the film roughness at the higher spatial frequencies is reduced faster than the one at the lower spatial frequencies, implying faster decay of the scattered intensity at higher $q_{||}$. Similar evolution of the out-of-plane scattering peaks from larger $q_{||}$ toward lower values could be observed during the island coalescence, caused by an increase in the mean distance between the nanostructures due to increasing island size.[27,30,31] However, the island coalescence typically appears at much higher spatial frequencies ($q_{||}$). In our case, the continuous decrease of $q_{||}$ during the deposition is related solely to mounded growth as the island coalescence appears ~3 min after the deposition, as will be discussed in more detail later in the text.

The calculated distance between perovskite islands from the reciprocal distance $2\Delta q_{||}$ between out-of-plane peaks at the beginning of growth is $D \approx 370$ nm. This value is close to the mean distance obtained by AFM ($D_{AFM} \approx 275$ nm). The difference between these two values can be explained by the fact that the overall scattering intensity is given by the product of the structure factor $S(q_{||})$ and the form factor $F(q)$.[31−33] $S(q_{||})$ describes the spatial arrangement of the scattering particles (i.e., islands), and their correlation and $F(q)$ is given by the particle shape. In our previous calculation, we calculated $D$ directly from the position of the out-of-plane diffraction, omitting the fact that its reciprocal position is also influenced by $F(q)$. The $F(q)$-function of the nanostructures shifts the peak position to lower values, which might inaccurately indicate the larger mean distance between the perovskite islands. Nevertheless, the $D$ value is important for


https://doi.org/10.1021/acs.jpclett.2c03422
J. Phys. Chem. Lett. 2022, 13, 11905−11912

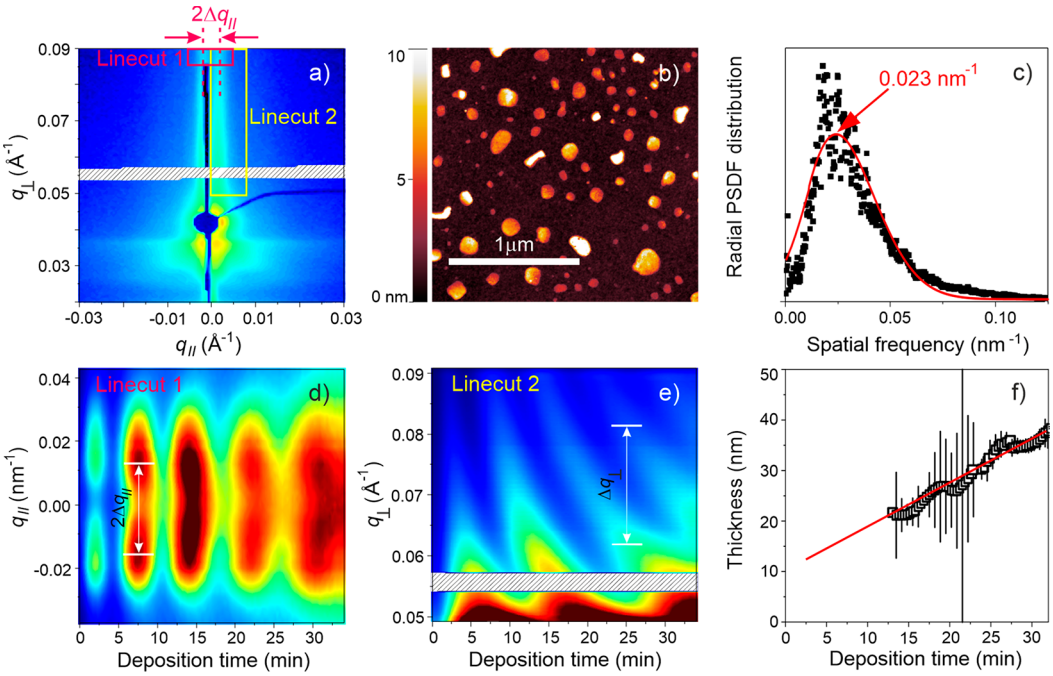


**Figure 2.** (a) GISAXS diffraction map containing information about the surface morphology. The reciprocal distance $2\Delta q_{||}$ between the out-of-plane scattering patterns, indicated by magenta dashed lines, corresponds to the inverse average island spacing. (b) AFM image of 2D perovskite islands and (c) a corresponding power spectral density function (PSDF) distribution calculated from the AFM image. The red curve indicates the fit by a Gaussian function with a maximum at 0.023 $nm^{-1}$. (d) and (e) Diffuse scattering along $q_{||}$ and $q_{\perp}$ directions during perovskite layer growth obtained from Linecut 1 and Linecut 2 indicated in (a), respectively. (f) Temporal perovskite layer thickness evolution, calculated from the reciprocal distance between two scattering intensity maxima indicated as $\Delta q_{\perp}$ in (e).

the final photovoltaic performance of the perovskite device since it defines the average grain size of the perovskite film. Several studies show that layers with large grains are more suitable for highly efficient photovoltaics.[34] It is worth noting that the grain size and overall morphology of the perovskite film are strongly affected by the substrate.[35,36] For the vapor-deposited perovskites, a high density of nuclei was observed on various (inorganic) substrates, leading to a small grain size typical for coevaporated perovskite films. It was also shown that the use of organic substrates could enhance the morphology and overall optoelectronic properties of the perovskite film.[35]

In addition, the GISAXS data provide information about the thickness of the deposited film. In conventional vacuum deposition, the layer thickness is typically deduced by monitoring the material deposited on the quartz crystal microbalance (QCM). However, this technique is not directly applicable to organic-based perovskites due to the volatile nature of the MAI precursor.[10,12,20,37] However, the deposited layer thickness can be inferred from the intensity oscillations along the diffuse scattering rod in the $q_{\perp}$ direction. Figure 2e shows the oscillations along $q_{\perp}$ in time. These oscillations are caused by the interference effects and shorten their period ($\Delta q_{\perp}$) due to the increasing thickness of perovskite film (same behavior as in Figure 2d). Analyzing the reciprocal distance between the intensity maxima for each deposition time, we were able to calibrate the perovskite film thickness, see Figure 2f, and the deposition rate of ∼1.4 nm/min. The layer thickness cannot be determined in the early stages of perovskite growth, as it does not form a continuous layer, but separated islands as discussed earlier. Within the accessible range in the $q_{\perp}$ direction, which is restricted by the experimental conditions, it was impossible to unambiguously determine at which time the coalescence of the islands occurs. The layer thickness could be obtained from ∼12 min after the deposition started. However, the moment of the coalescence—when the grains begin to touch—could be deduced indirectly from the PL measurements, as explained later in the text.

To investigate the evolution of the $MAPbI_3$ crystallographic properties, the GIWAXS patterns were recovered. Research on the vapor-based deposition of perovskites is not predominantly focused on the crystallographic variations of the structure during growth, presumably due to the need for a custom-designed system. In most studies, the diffraction patterns are used to determine the crystal phases, i.e., tetragonal or cubic, while changing external parameters, such as the working pressure, precursor temperature, or substrate temperature.[12,20,37−40] Here, we investigated the changes in the crystallographic structure during $MAPbI_3$ growth in a vacuum.

Figure 3 shows the GIWAXS reciprocal space map obtained at the end of the $MAPbI_3$ deposition (layer thickness ∼37 nm). The positions of the diffraction peaks are consistent with the tetragonal crystal structure typically observed for $MAPbI_3$ at room temperature.[41−43] Our GIWAXS pattern indicates good film quality with no excessive amount of any of the precursors observed. The perovskite layer is composed of monocrystalline domains (grains) that mostly exhibit one preferential crystallographic orientation with the (001) lattice planes parallel to the substrate surface. This feature is in stark contrast to the grain orientation obtained for solution-based techniques, where the grains are typically randomly oriented.[44] Furthermore, we have chosen the 002 and 110 diffraction peaks and analyzed their evolution during perovskite deposition by fitting with Gaussians (see Figure S2). These diffraction peaks were selected because they are the most intense ones and thus can be analyzed from the early stages of $MAPbI_3$ growth.


https://doi.org/10.1021/acs.jpclett.2c03422
J. Phys. Chem. Lett. 2022, 13, 11905−11912

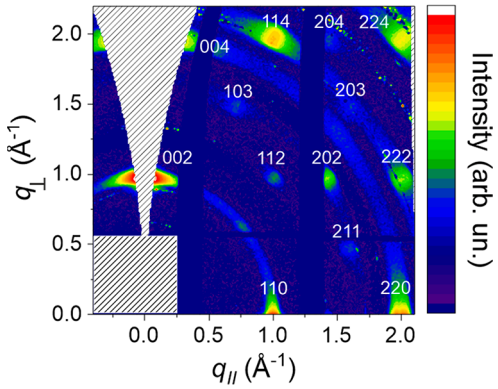


**Figure 3.** GIWAXS reciprocal diffraction map taken at the end of the MAPbI growth (deposition time = 34 min, layer thickness ∼37 nm). The diffraction peaks from the corresponding lattice planes are labeled. The detected scattering intensity is colored on a logarithmic scale to highlight less intense diffraction peaks. The color scale indicates the intensity increase from blue to red.

Additionally, 002 and 110 diffraction peaks provide information on all three lattice parameters *a*, *b*, and *c*; i.e., the unit cell evolution can be studied in all three spatial directions.

Moreover, we aim to correlate the structural properties of the perovskite layer with the electronic ones. So before further investigating the structural properties obtained by GIWAXS, we now turn to results acquired from the PL measurements. Figure 4 shows the heat map of the PL intensity measured during $MAPbI_3$ deposition. The spectra were fitted by the PseudoVoigt function as it matched the spectral profiles well. The obtained spectral position of the PL peak, indicated as a dashed line in Figure 4a, continuously redshifts from higher energies ∼1.95 eV at the beginning of the growth toward ∼1.63 eV for thicker layers, which is a typical emission of evaporated $MAPbI_3$.[21,44−46] The PL shift can be attributed to the strong quantum confinement effects at the beginning of growth, where crystallites of a few nanometers are formed.[47−49] According to the theoretical calculations by Anaya et al.[47] and Zhang et al.,[48] the PL peak position of 1.95 eV corresponds to a nanocrystallite size of ∼6 nm. The emission continuously redshifts during the deposition due to the gradual enlargement of $MAPbI_3$ crystallites. The redshifting of PL during the layer formation was also observed for the solution-processed $MAPbI_3$;[44−46,50] however, the total energy shifts did not exceed 0.15 eV. In contrast, here we observed an overall PL peak shift of ∼0.32 eV, covering the emission from $MAPbI_3$ quantum dots to a closed layer. For comparison, Parrot et al.[51] reported a redshift for coevaporated layers where the PL spectra were measured *ex situ* for various $MAPbI_3$ thicknesses. The PL peak was red-shifted ∼0.1 eV from crystallite islands of a few-nanometer size to ∼100 nm film thickness.

PL intensity analysis in Figure 4b shows a rapid emission increase at the beginning of perovskite growth up to its maximum value (∼3 min after the deposition started), followed by a slower decrease. A similar PL intensity evolution was recently observed for solution-processed perovskites during annealing[45,46,50] and assigned to the formation of surface defects and grain boundaries.[44] Despite the absence of the liquid phase in vapor-based deposition, the PL intensity character is the same for vapor and solution-based techniques. Based on the overall PL evolution, we can distinguish three different stages of $MAPbI_3$ crystallization.

*Stage I: Formation of perovskite grains.* In the first stage of perovskite deposition, small nanocrystallites are formed, continuously growing as more material is deposited (see Figure 4d). This stage is characterized by the PL intensity increase, reaching its peak at ∼3 min of deposition. The redshifting of the PL peak position is fast due to the growth of perovskite crystallites in all three directions. The growth of the perovskite phase can also be confirmed by the increasing 002 diffraction intensity in Figure 4c. Interestingly, we observe a rapid change in the 002 peak position during this stage of

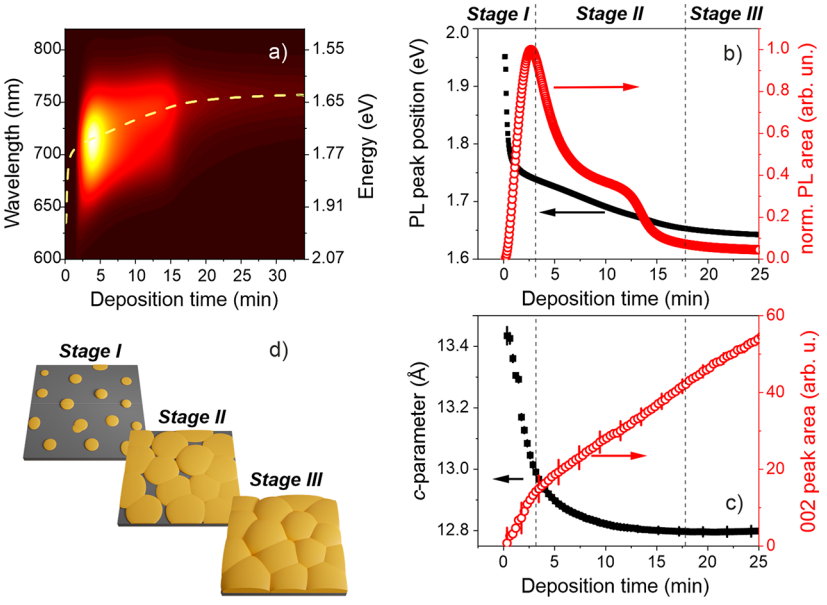


**Figure 4.** (a) Heat map of spectrally resolved photoluminescence (PL) obtained during $MAPbI_3$ deposition. The yellow dashed line indicates the PL peak position. (b and c) Comparison of selected parameters and their time evolution. (b) Time evolution of PL peak area and position and (c) GIWAXS 002 peak area and $MAPbI_3$ lattice parameter *c*. The gray dashed lines in (b) and (c) indicate the three different stages of $MAPbI_3$ growth that are described in the text and schematically depicted in (d).



https://doi.org/10.1021/acs.jpclett.2c03422
J. Phys. Chem. Lett. 2022, 13, 11905−11912

perovskite growth (Figure S2), which represents a shrinkage of the unit cell *c*-parameter (see Figure 4c). A significant reduction of *c* can be explained by a strain induced by the rapid growth of perovskite grains. The overall decrease of the *c*-parameter is $\Delta c/c \approx 4.5\%$, with respect to its steady value at the end of the layer growth, where $c = 12.8 \pm 0.1$ Å. In our case, the growth-induced compressive strain acts mainly in the vertical direction and translates into shrinkage of the unit cell *c*-parameter, whereas *a* and *b* do not change substantially. We note that only a minor change in *a* and *b* of ±0.3%, i.e., within the experimental error, was obtained from the reciprocal position of the 110 peak in Figure S2.

Previously, the origin of the strain was explained by the thermally induced cubic-to-tetragonal phase transitions in solution-based perovskites.[52,53] For solution-based films, the high processing temperatures of ∼100 °C are used, and the perovskites undergo such a phase transition (at ∼57 °C) during cooling to room temperature. In our experiment, the substrate was kept at room temperature throughout the deposition, so the cubic-to-tetragonal transition as the cause of the strain is very unlikely. Additionally, no transition in the GIWAXS pattern was observed during perovskite growth.

*Stage II: Formation of defects*. This stage is characterized by a significant PL quenching. Such a PL intensity decrease was observed previously during perovskite formation,[45,46,50,54] but its origin was not fully explained. Song et al.[46] speculated that the gradual drop of PL intensity is caused by photodarkening and thermally induced effects. However, the thermally induced PL quenching is unlikely, as the intensity of the laser diode in our experiment was set low to overcome the thermally driven bleaching effects, and although the photodarkening effects were previously observed in optical fibers,[55] no relevant evidence was provided to support the assumption of this hypothesis in perovskites.

We suggest that the PL quenching can be explained by the coalescence of individual perovskite crystallites. The coalescence was confirmed by AFM images of the $MAPbI_3$ layer obtained at the time when the PL intensity had just started to decrease (see Figure S1). This assumption is also accompanied by a slower redshift of the PL peak than in *Stage I* as the perovskite growth continues only in the direction perpendicular to the substrate plane. The grain boundaries between the crystallites act as defects and sources of nonradiative PL recombination.[56−59] The formation of nonradiative defects is one of the major obstacles in achieving the highest possible power conversion efficiency, as they decrease the quasi-Fermi-level splitting that limits the open-circuit voltage of the solar cells.[60−62] Thus, this stage (*II*) can be considered the most critical in perovskite film formation. Various passivation strategies, exploiting organic or inorganic molecules to precipitate at grain boundaries, can be applied to mitigate the nonradiative recombinations.[63,64]

Recently, a correlation between growth-induced strain and nonradiative recombinations was observed by Jones et al.[52] They observed that growth-induced lattice strain is directly linked with a greater defect concentration and hence with PL decay. A similar observation was also done by Jariwala et al., who focused on measuring local strain within a perovskite grain.[65] On the contrary, although our experiment allows measuring the strain averaged over a millimeter-sized area, such an unambiguous correlation between PL quenching and compressive strain cannot be made. On the one hand, the compressive strain, as evidenced by the *c*-parameter decrease, is present in *Stage II* along with the PL intensity decrease. On the other hand, a significantly greater strain did not have a large effect on the PL amplitude during $MAPbI_3$ grain formation *Stage I*. Hence, our measurements suggest that the growth-induced compressive strain does not have a major influence on the overall PL signal.

Interestingly, the 002 diffraction intensity seems to slow down in *Stage II* (compared to *Stage I*), although the precursors' flux is approximately constant during deposition. However, this apparent intensity deceleration is caused by a change in the texture of the polycrystalline film. In *Stage I*, the perovskite islands are randomly oriented in the sample plane, having some orientation deviation in the out-of-plane direction. The out-of-plane misorientation is, in fact, a tilt of the crystallites' *c*-axes. Such tilt is evident in the broadening of the 002 diffraction peak in the in-plane direction (see Figure S3). After the crystallite coalescence in *Stage II*, the texture of the perovskite layer becomes more homogeneous, leading to a narrowing of the 002 peak. Consequently, the 002 peak coincides more with a *missing wedge* (see Figure 3), causing an illusive decrease in the peak intensity. In contrast, no such change in intensity slope was observed for the 110 diffraction peak because its position in reciprocal space is far from the *missing wedge*.

*Stage III: Steady perovskite layer growth*. The final stage of $MAPbI_3$ growth is characterized by a steady PL peak position (∼1.63 eV) and a constant value of the *c*-parameter (see Figure 4b,c). Such stable growth was observed after ∼17 min of the deposition. Although $MAPbI_3$ deposition continues with an almost steady flux of the precursors, the PL and GIWAXS intensities have different behaviors. The GIWAXS intensity keeps increasing monotonically, while the PL signal remains constant. Such distinct behavior is caused by different absorption coefficients (and thus penetration depths) for the 405 nm excitation wavelength and the X-ray beam. For the X-rays ($\lambda_{X\text{-ray}} = 1.05$ Å; $E_{X\text{-ray}} = 11.83$ keV), the penetration depth is ∼50 nm. So, unless the perovskite layer thickness is not greater than 50 nm (for the X-ray incident angle of 0.2°, see Experimental methods in the Supporting Information), the GIWAXS intensity will increase as more material is deposited. However, for the excitation laser ($\lambda_{ex} = 405$ nm; $E_{ex} = 3.06$ eV), the penetration depth is only ∼30 nm.[66−68] We calculated that the $MAPbI_3$ thickness is (26 ± 4) nm after 17 min of deposition (see Figure 2f). Thus, from this moment on, the laser excites the same perovskite volume despite the increasing layer thickness, and the PL intensity remains constant.

In summary, we studied the formation of $MAPbI_3$ perovskite employing vapor deposition. The development of $MAPbI_3$ from a few nanometer-size crystallites up to a closed layer was characterized in terms of structural and optoelectronic properties by using *in-situ* GI-SAXS/WAXS and PL simultaneously. We observed that the growth of $MAPbI_3$ nanocrystals is manifested in rapid PL intensity increase and a substantial PL redshift. At the same time, the growth-induced compressive strain leads to a rapid decrease of the unit cell volume, predominantly given by the shrinkage of the *c*-parameter. Contrary to previous reports, we identified that the subsequent strain release does not influence the nonradiative recombination significantly. Furthermore, the formation of a continuous perovskite layer results in the development of defects on the grain boundaries, which quenches the PL signal. Interestingly, the PL evolution is remarkably similar to $MAPbI_3$ formation from solvent precursors observed in refs 44, 45, and 54. We


https://doi.org/10.1021/acs.jpclett.2c03422
J. Phys. Chem. Lett. 2022, 13, 11905−11912

believe that further work is required, especially for vapor-deposited perovskites, to understand the complex connection between structure and emission efficiency. Such research is inevitable for optimizing the perovskite growth process and achieving highly efficient films on a large scale.

## ■ ASSOCIATED CONTENT

### Supporting Information

The Supporting Information is available free of charge at https://pubs.acs.org/doi/10.1021/acs.jpclett.2c03422.

Experimental methods, AFM images, and complementary PL data and GI-SAXS/WAXS data (PDF)

Transparent Peer Review report available (PDF)

## ■ AUTHOR INFORMATION


### Corresponding Author

**Nada Mrkyvkova** − *Institute of Physics, Slovak Academy of Sciences, 845 11 Bratislava, Slovakia; Center for Advanced Materials Application, Slovak Academy of Sciences, 845 11 Bratislava, Slovakia;* orcid.org/0000-0002-2619-0872; Email: nada.mrkyvkova@savba.sk

### Authors

**Vladimir Held** − *Institute of Physics, Slovak Academy of Sciences, 845 11 Bratislava, Slovakia*

**Peter Nádaždy** − *Institute of Physics, Slovak Academy of Sciences, 845 11 Bratislava, Slovakia; Center for Advanced Materials Application, Slovak Academy of Sciences, 845 11 Bratislava, Slovakia*

**Karol Vegso** − *Institute of Physics, Slovak Academy of Sciences, 845 11 Bratislava, Slovakia; Center for Advanced Materials Application, Slovak Academy of Sciences, 845 11 Bratislava, Slovakia;* orcid.org/0000-0003-2595-6036

**Aleš Vlk** − *Laboratory of Thin Films, Institute of Physics, ASCR, 162 00 Prague, Czech Republic;* orcid.org/0000-0003-2866-7133

**Martin Ledinský** − *Laboratory of Thin Films, Institute of Physics, ASCR, 162 00 Prague, Czech Republic;* orcid.org/0000-0002-6586-5473

**Matej Jergel** − *Institute of Physics, Slovak Academy of Sciences, 845 11 Bratislava, Slovakia; Center for Advanced Materials Application, Slovak Academy of Sciences, 845 11 Bratislava, Slovakia;* orcid.org/0000-0002-4482-7881

**Andrei Chumakov** − *Photon Science, Deutsches Elektronen-Synchrotron (DESY), Hamburg 22607, Germany;* orcid.org/0000-0003-3195-9356

**Stephan V. Roth** − *Photon Science, Deutsches Elektronen-Synchrotron (DESY), Hamburg 22607, Germany;* orcid.org/0000-0002-6940-6012

**Frank Schreiber** − *Institute of Applied Physics, University of Tübingen, 72076 bingen, Germany;* orcid.org/0000-0003-3659-6718

**Peter Siffalovic** − *Institute of Physics, Slovak Academy of Sciences, 845 11 Bratislava, Slovakia; Center for Advanced Materials Application, Slovak Academy of Sciences, 845 11 Bratislava, Slovakia;* orcid.org/0000-0002-9807-0810

Complete contact information is available at: https://pubs.acs.org/10.1021/acs.jpclett.2c03422


### Notes

The authors declare no competing financial interest.

## ■ ACKNOWLEDGMENTS

We acknowledge the financial support of projects APVV-21-0297, SK-CZ-RD-21-0043, APVV-17-0352, APVV-19-0465, APVV-20-0111, SK-AT-20-0006, VEGA 2/0046/21, VEGA 2/0041/21, ITMS 26230120002, ITMS 26210120002, and ITMS 26210120023. This work was performed during the implementation of the project Building-up Centre for Advanced Materials Application of the Slovak Academy of Sciences, ITMS project code 313021T081, supported by the Research & Innovation Operational Programme funded by the ERDF. The authors also acknowledge the support by the BMBF and DFG, together with the Operational Programme Research, Development, Education financed by the European Structural and Investment Funds, the Czech Ministry of Education, Youth and Sports (Project No. CZ.02.1.01/0.0/0.0/16_019/0000760_SOLID21, LUASK 22202, and Czech-NanoLab Research Infrastructure LM2018110). Furthermore, we acknowledge Dr. Alina Vlad and Dr. Alessandro Coati from the Soleil synchrotron, where the preliminary GIWAXS and PL results were obtained at the SIXS beamline. We acknowledge DESY (Hamburg, Germany), a member of the Helmholtz Association HGF, for providing experimental facilities. Parts of this research were carried out at PETRA III, and we would like to thank P03 beamline staff for the assistance.

## ■ REFERENCES


(1) Correa-Baena, J. P.; Saliba, M.; Buonassisi, T.; Grätzel, M.; Abate, A.; Tress, W.; Hagfeldt, A. Promises and Challenges of Perovskite Solar Cells. *Science* **2017**, *358* (6364), 739−744.

(2) Chen, Q.; De Marco, N.; Yang, Y.; Song, T.-B.; Chen, C. C.; Zhao, H.; Hong, Z.; Zhou, H.; Yang, Y. Under the Spotlight: The Organic-Inorganic Hybrid Halide Perovskite for Optoelectronic Applications. *Nano Today* **2015**, *10* (3), 355−396.

(3) Jeong, M.; Choi, I. W.; Go, E. M.; Cho, Y.; Kim, M.; Lee, B.; Jeong, S.; Jo, Y.; Choi, H. W.; Lee, J.; et al. Stable Perovskite Solar Cells with Efficiency Exceeding 24.8% and 0.3-V Voltage Loss. *Science* **2020**, *369* (6511), 1615−1620.

(4) Schmidt-Mende, L.; Dyakonov, V.; Olthof, S.; Ünlü, F.; Lê, K. M. T.; Mathur, S.; Karabanov, A. D.; Lupascu, D. C.; Herz, L. M.; Hinderhofer, A.; et al. Roadmap on Organic-Inorganic Hybrid Perovskite Semiconductors and Devices. *APL Materials* **2021**, *9* (10), 109202.

(5) Arora, N.; Dar, M. I.; Hinderhofer, A.; Pellet, N.; Schreiber, F.; Zakeeruddin, S. M.; Grätzel, M. Perovskite Solar Cells with CuSCN Hole Extraction Layers Yield Stabilized Efficiencies Greater than 20. *Science* **2017**, *358* (6364), 768−771.

(6) Brinkmann, K. O.; Becker, T.; Zimmermann, F.; Kreusel, C.; Gahlmann, T.; Theisen, M.; Haeger, T.; Olthof, S.; Tückmantel, C.; Günster, M.; et al. Perovskite−Organic Tandem Solar Cells with Indium Oxide Interconnect. *Nature* **2022**, *604* (7905), 280−286.

(7) Min, H.; Lee, D. Y.; Kim, J.; Kim, G.; Lee, K. S.; Kim, J.; Paik, M. J.; Kim, Y. K.; Kim, K. S.; Kim, M. G.; et al. Perovskite Solar Cells with Atomically Coherent Interlayers on SnO2 Electrodes. *Nature* **2021**, *598* (7881), 444−450.

(8) Jeong, J.; Kim, M.; Seo, J.; Lu, H.; Ahlawat, P.; Mishra, A.; Yang, Y.; Hope, M. A.; Eickemeyer, F. T.; Kim, M.; et al. Pseudo-Halide Anion Engineering for $\alpha$-FAPbI3 Perovskite Solar Cells. *Nature* **2021**, *592* (7854), 381−385.

(9) Wang, S.; Li, X.; Wu, J.; Wen, W.; Qi, Y. Fabrication of Efficient Metal Halide Perovskite Solar Cells by Vacuum Thermal Evaporation: A Progress Review. *Current Opinion in Electrochemistry* **2018**, *11*, 130−140.

(10) Ono, L. K.; Leyden, M. R.; Wang, S.; Qi, Y. Organometal Halide Perovskite Thin Films and Solar Cells by Vapor Deposition. *Journal of Materials Chemistry A* **2016**, *4* (18), 6693−6713.

(11) Borchert, J.; Levchuk, I.; Snoek, L. C.; Rothmann, M. U.; Haver, R.; Snaith, H. J.; Brabec, C. J.; Herz, L. M.; Johnston, M. B. Impurity Tracking Enables Enhanced Control and Reproducibility of Hybrid Perovskite Vapor Deposition. *ACS Appl. Mater. Interfaces* **2019**, *11* (32), 28851−28857.
(12) Castro-Méndez, A. F.; Perini, C. A. R.; Hidalgo, J.; Ranke, D.; Vagott, J. N.; An, Y.; Lai, B.; Luo, Y.; Li, R.; Correa-Baena, J. P. Formation of a Secondary Phase in Thermally Evaporated MAPbI3 and Its Effects on Solar Cell Performance. *ACS Appl. Mater. Interfaces* **2022**, *14*, 34269.
(13) Yilbas, B. S.; Al-Sharafi, A.; Ali, H.Chapter 3 - Surfaces for Self-Cleaning. In *Self-Cleaning of Surfaces and Water Droplet Mobility*; Yilbas, B. S., Al-Sharafi, A., Ali, H., Eds.; Elsevier, 2019; pp 45−98.
(14) Hamukwaya, S. L.; Hao, H.; Zhao, Z.; Dong, J.; Zhong, T.; Xing, J.; Hao, L.; Mashingaidze, M. M. A Review of Recent Developments in Preparation Methods for Large-Area Perovskite Solar Cells. *Coatings* **2022**, *12*, 252.
(15) Vaynzof, Y. The Future of Perovskite Photovoltaics—Thermal Evaporation or Solution Processing? *Adv. Energy Mater.* **2020**, *10* (48), 2003073.
(16) Loper, P.; Niesen, B.; Moon, S. J.; Martin De Nicolas, S.; Holovsky, J.; Remes, Z.; Ledinsky, M.; Haug, F. J.; Yum, J. H.; De Wolf, S.; et al. Organic-Inorganic Halide Perovskites: Perspectives for Silicon-Based Tandem Solar Cells. *IEEE Journal of Photovoltaics* **2014**, *4* (6), 1545−1551.
(17) Liu, N.; Wang, L.; Xu, F.; Wu, J.; Song, T.; Chen, Q. Recent Progress in Developing Monolithic Perovskite/Si Tandem Solar Cells. *Frontiers in Chemistry* **2020**, *8* (December), 1−22.
(18) Antrack, T.; Kroll, M.; Sudzius, M.; Cho, C.; Imbrasas, P.; Albaladejo-Siguan, M.; Benduhn, J.; Merten, L.; Hinderhofer, A.; Schreiber, F.; Reineke, S.; Vaynzof, Y.; Leo, K. Optical Properties of Perovskite-Organic Multiple Quantum Wells. *Advanced Science* **2022**, *9* (24), 2200379.
(19) Lin, R.; Xu, J.; Wei, M.; Wang, Y.; Qin, Z.; Liu, Z.; Wu, J.; Xiao, K.; Chen, B.; Park, S. M.; et al. All-Perovskite Tandem Solar Cells with Improved Grain Surface Passivation. *Nature* **2022**, *603* (7899), 73−78.
(20) Lohmann, K. B.; Patel, J. B.; Rothmann, M. U.; Xia, C. Q.; Oliver, R. D. J.; Herz, L. M.; Snaith, H. J.; Johnston, M. B. Control over Crystal Size in Vapor Deposited Metal-Halide Perovskite Films. *ACS Energy Letters* **2020**, *5* (3), 710−717.
(21) Teuscher, J.; Ulianov, A.; Müntener, O.; Grätzel, M.; Tétreault, N. Control and Study of the Stoichiometry in Evaporated Perovskite Solar Cells. *ChemSusChem* **2015**, *8* (22), 3847−3852.
(22) Gil-Escrig, L.; Roß, M.; Sutter, J.; Al-Ashouri, A.; Becker, C.; Albrecht, S. Fully Vacuum-Processed Perovskite Solar Cells on Pyramidal Microtextures. *Solar RRL* **2021**, *5* (1), 2000553.
(23) Ugur, E.; Alarousu, E.; Khan, J. I.; Vlk, A.; Aydin, E.; De Bastiani, M.; Balawi, A. H.; Gonzalez Lopez, S. P.; Ledinský, M.; De Wolf, S.; et al. How Humidity and Light Exposure Change the Photophysics of Metal Halide Perovskite Solar Cells. *Solar RRL* **2020**, *4* (11), 2000382.
(24) Mrkyvkova, N.; Held, V.; Halahovets, Y.; Nádaždy, P.; Jergel, M.; Majková, E.; Schreiber, F.; Siffalovic, P. Simultaneous Measurement of X-Ray Scattering and Photoluminescence during Molecular Deposition. *J. Lumin.* **2022**, *248*, 118950.
(25) Yang, J.; Siempelkamp, B. D.; Liu, D.; Kelly, T. L. Investigation of CH3NH3PbI3 Degradation Rates and Mechanisms in Controlled Humidity Environments Using in Situ Techniques. *ACS Nano* **2015**, *9* (2), 1955−1963.
(26) Xu, W.; Li, F.; Cai, Z.; Wang, Y.; Luo, F.; Chen, X. An Ultrasensitive and Reversible Fluorescence Sensor of Humidity Using Perovskite CH3NH3PbBr3. *Journal of Materials Chemistry C* **2016**, *4* (41), 9651−9655.
(27) Schwartzkopf, M.; Buffet, A.; Korstgens, V.; Metwalli, E.; Schlage, K.; Benecke, G.; Perlich, J.; Rawolle, M.; Rothkirch, A.; Heidmann, B.; Herzog, G.; Muller-Buschbaum, P.; Rohlsberger, R.; Gehrke, R.; Stribeck, N.; Roth, S. V. From Atoms to Layers: In Situ Gold Cluster Growth Kinetics during Sputter Deposition. *Nanoscale* **2013**, *5* (11), 5053.
(28) Bommel, S.; Kleppmann, N.; Weber, C.; Spranger, H.; Schäfer, P.; Novak, J.; Roth, S. V.; Schreiber, F.; Klapp, S. H. L.; Kowarik, S. Unravelling the Multilayer Growth of the Fullerene C 60 in Real Time. *Nat. Commun.* **2014**, *5*, 5388.
(29) Pelliccione, M.; Lu, T.-M.*Evolution of Thin Film Morphology: Modeling and Simulations*; Springer, 2008.
(30) Santoro, G.; Yu, S.; Schwartzkopf, M.; Zhang, P.; Koyiloth Vayalil, S.; Risch, J. F. H.; Rübhausen, M. A.; Hernández, M.; Domingo, C.; Roth, S. V. Silver Substrates for Surface Enhanced Raman Scattering: Correlation between Nanostructure and Raman Scattering Enhancement. *Appl. Phys. Lett.* **2014**, *104* (24), 243107.
(31) Santoro, G.; Yu, S.Grazing Incidence Small Angle X-Ray Scattering as a Tool for In- Situ Time-Resolved Studies. In *X-ray Scattering*; Ares, A. E., Ed.; IntechOpen, 2017.
(32) Schnablegger, H.; Singh, Y.*The SAXS Guide*; 2011.
(33) Jeffries, C. M.; Ilavsky, J.; Martel, A.; Hinrichs, S.; Meyer, A.; Pedersen, J. S.; Sokolova, A. V.; Svergun, D. I. Small-Angle X-Ray and Neutron Scattering. *Nature Reviews Methods Primers* **2021**, *1*, 70.
(34) Peter Amalathas, A.; Landová, L.; Hájková, Z.; Horák, L.; Ledinsky, M.; Holovský, J. Controlled Growth of Large Grains in CH3NH3PbI3Perovskite Films Mediated by an Intermediate Liquid Phase without an Antisolvent for Efficient Solar Cells. *ACS Applied Energy Materials* **2020**, *3* (12), 12484−12493.
(35) Abzieher, T.; Feeney, T.; Schackmar, F.; Donie, Y. J.; Hossain, I. M.; Schwenzer, J. A.; Hellmann, T.; Mayer, T.; Powalla, M.; Paetzold, U. W. From Groundwork to Efficient Solar Cells: On the Importance of the Substrate Material in Co-Evaporated Perovskite Solar Cells. *Adv. Funct. Mater.* **2021**, *31* (42), 2104482.
(36) Olthof, S.; Meerholz, K. Substrate-Dependent Electronic Structure and Film Formation of MAPbI 3 Perovskites. *Sci. Rep.* **2017**, *7* (January), 40267.
(37) Kim, B. S.; Choi, M. H.; Choi, M. S.; Kim, J. J. Composition-Controlled Organometal Halide Perovskite Via CH3NH3I Pressure in a Vacuum Co-Deposition Process. *Journal of Materials Chemistry A* **2016**, *4* (15), 5663−5668.
(38) Palazon, F.; Pérez-del-Rey, D.; Dänekamp, B.; Dreessen, C.; Sessolo, M.; Boix, P. P.; Bolink, H. J. Room-Temperature Cubic Phase Crystallization and High Stability of Vacuum-Deposited Methylammonium Lead Triiodide Thin Films for High-Efficiency Solar Cells. *Adv. Mater.* **2019**, *31* (39), 1902692.
(39) Pistor, P.; Borchert, J.; Fränzel, W.; Csuk, R.; Scheer, R. Monitoring the Phase Formation of Coevaporated Lead Halide Perovskite Thin Films by in Situ X-Ray Diffraction. *J. Phys. Chem. Lett.* **2014**, *5* (19), 3308−3312.
(40) Borchert, J.; Boht, H.; Fränzel, W.; Csuk, R.; Scheer, R.; Pistor, P. Structural Investigation of Co-Evaporated Methyl Ammonium Lead Halide Perovskite Films during Growth and Thermal Decomposition Using Different PbX2 (X = I, Cl) Precursors. *Journal of Materials Chemistry A* **2015**, *3* (39), 19842−19849.
(41) Malinkiewicz, O.; Yella, A.; Lee, Y. H.; Espallargas, G. M.; Graetzel, M.; Nazeeruddin, M. K.; Bolink, H. J. Perovskite Solar Cells Employing Organic Charge-Transport Layers. *Nat. Photonics* **2014**, *8* (2), 128−132.
(42) Quarti, C.; Mosconi, E.; Ball, J. M.; D'Innocenzo, V.; Tao, C.; Pathak, S.; Snaith, H. J.; Petrozza, A.; De Angelis, F. Structural and Optical Properties of Methylammonium Lead Iodide across the Tetragonal to Cubic Phase Transition: Implications for Perovskite Solar Cells. *Energy Environ. Sci.* **2016**, *9* (1), 155−163.
(43) Kawamura, Y.; Mashiyama, H.; Hasebe, K. Structural Study on Cubic-Tetragonal Transition of CH3NH 3PbI3. *J. Phys. Soc. Jpn.* **2002**, *71* (7), 1694.
(44) Mrkyvkova, N.; Held, V.; Nádaždy, P.; Subair, R.; Majkova, E.; Jergel, M.; Vlk, A.; Ledinsky, M.; Kotlár, M.; Tian, J.; et al. Combined in Situ Photoluminescence and X-Ray Scattering Reveals Defect Formation in Lead-Halide Perovskite Films. *J. Phys. Chem. Lett.* **2021**, *12* (41), 10156−10162.


https://doi.org/10.1021/acs.jpclett.2c03422
J. Phys. Chem. Lett. 2022, 13, 11905−11912

(45) Suchan, K.; Just, J.; Becker, P.; Unger, E. L.; Unold, T. Optical: In Situ Monitoring during the Synthesis of Halide Perovskite Solar Cells Reveals Formation Kinetics and Evolution of Optoelectronic Properties. *Journal of Materials Chemistry A* **2020**, *8* (20), 10439.
(46) Song, T.-B.; Yuan, Z.; Mori, M.; Motiwala, F.; Segev, G.; Masquelier, E.; Stan, C. V.; Slack, J. L.; Tamura, N.; Sutter-Fella, C. M. Revealing the Dynamics of Hybrid Metal Halide Perovskite Formation via Multimodal In Situ Probes. *Adv. Funct. Mater.* **2020**, *30* (6), 1908337.
(47) Anaya, M.; Rubino, A.; Rojas, T. C.; Galisteo-López, J. F.; Calvo, M. E.; Míguez, H. Strong Quantum Confinement and Fast Photoemission Activation in CH3NH3PbI3 Perovskite Nanocrystals Grown within Periodically Mesostructured Films. *Advanced Optical Materials* **2017**, *5* (8), 1601087.
(48) Zhang, F.; Huang, S.; Wang, P.; Chen, X.; Zhao, S.; Dong, Y.; Zhong, H. Colloidal Synthesis of Air-Stable CH3NH3PbI3 Quantum Dots by Gaining Chemical Insight into the Solvent Effects. *Chem. Mater.* **2017**, *29* (8), 3793−3799.
(49) Malgras, V.; Tominaka, S.; Ryan, J. W.; Henzie, J.; Takei, T.; Ohara, K.; Yamauchi, Y. Observation of Quantum Confinement in Monodisperse Methylammonium Lead Halide Perovskite Nanocrystals Embedded in Mesoporous Silica. *J. Am. Chem. Soc.* **2016**, *138* (42), 13874−13881.
(50) Wagner, L.; Mundt, L. E.; Mathiazhagan, G.; Mundus, M.; Schubert, M. C.; Mastroianni, S.; Würfel, U.; Hinsch, A.; Glunz, S. W. Distinguishing Crystallization Stages and Their Influence on Quantum Efficiency during Perovskite Solar Cell Formation in Real-Time. *Sci. Rep.* **2017**, *7* (1), 1−6.
(51) Parrott, E. S.; Patel, J. B.; Haghighirad, A. A.; Snaith, H. J.; Johnston, M. B.; Herz, L. M. Growth Modes and Quantum Confinement in Ultrathin Vapour-Deposited MAPbI3 Films. *Nanoscale* **2019**, *11* (30), 14276.
(52) Jones, T. W.; Osherov, A.; Alsari, M.; Sponseller, M.; Duck, B. C.; Jung, Y. K.; Settens, C.; Niroui, F.; Brenes, R.; Stan, C. V.; et al. Lattice Strain Causes Non-Radiative Losses in Halide Perovskites. *Energy Environ. Sci.* **2019**, *12* (2), 596−606.
(53) Zhao, J.; Deng, Y.; Wei, H.; Zheng, X.; Yu, Z.; Shao, Y.; Shield, J. E.; Huang, J.Strained Hybrid Perovskite Thin Films and Their Impact on the Intrinsic Stability of Perovskite Solar Cells. *Science Advances***2017**, *3* (11). DOI: 10.1126/sciadv.aao5616
(54) Song, T.-B.; Yuan, Z.; Babbe, F.; Nenon, D. P.; Aydin, E.; De Wolf, S.; Sutter-Fella, C. M. Dynamics of Antisolvent Processed Hybrid Metal Halide Perovskites Studied by In Situ Photoluminescence and Its Influence on Optoelectronic Properties. *ACS Applied Energy Materials* **2020**, *3* (3), 2386−2393.
(55) Taccheo, S.; Gebavi, H.; Tregoat, D.; Robin, T.; Cadier, B.; Milanese, D.; Leick, L. Photodarkening: Measure, Characterization, and Figure of Merit. *SPIE Newsroom* **2012**, 10−12.
(56) Adhyaksa, G. W. P.; Brittman, S.; Abolins, H.; Lof, A.; Li, X.; Keelor, J. D.; Luo, Y.; Duevski, T.; Heeren, R. M. A.; Ellis, S. R.; Fenning, D. P.; Garnett, E. C. Understanding Detrimental and Beneficial Grain Boundary Effects in Halide Perovskites. *Adv. Mater.* **2018**, *30*, 1804792.
(57) DeQuilettes, D. W.; Zhang, W.; Burlakov, V. M.; Graham, D. J.; Leijtens, T.; Osherov, A.; Bulović, V.; Snaith, H. J.; Ginger, D. S.; Stranks, S. D. Photo-Induced Halide Redistribution in Organic-Inorganic Perovskite Films. *Nat. Commun.* **2016**, *7*, 11683.
(58) Kim, D.; Higgins, K.; Ahmadi, M. Navigating Grain Boundaries in Perovskite Solar Cells. *Matter* **2021**, *4* (5), 1442−1445.
(59) Park, J. S.; Calbo, J.; Jung, Y. K.; Whalley, L. D.; Walsh, A. Accumulation of Deep Traps at Grain Boundaries in Halide Perovskites. *ACS Energy Letters* **2019**, *4* (6), 1321−1327.
(60) Luo, D.; Su, R.; Zhang, W.; Gong, Q.; Zhu, R. Minimizing Non-Radiative Recombination Losses in Perovskite Solar Cells. *Nature Reviews Materials* **2020**, *5*, 44−60.
(61) Ledinsky, M.; Vlk, A.; Schonfeldova, T.; Holovsky, J.; Aydin, E.; Dang, H. X.; Hajkova, Z.; Landova, L.; Valenta, J.; Fejfar, A.; et al. Impact of Cation Multiplicity on Halide Perovskite Defect Densities and Solar Cell Voltages. *J. Phys. Chem. C* **2020**, *124* (50), 27333−27339.
(62) Braly, I. L.; Dequilettes, D. W.; Pazos-Outón, L. M.; Burke, S.; Ziffer, M. E.; Ginger, D. S.; Hillhouse, H. W. Hybrid Perovskite Films Approaching the Radiative Limit with over 90% Photoluminescence Quantum Efficiency. *Nat. Photonics* **2018**, *12* (6), 355−361.
(63) Ye, J.; Byranvand, M. M.; Martínez, C. O.; Hoye, R. L.; Saliba, M.; Polavarapu, L. Defect Passivation in Lead-Halide Perovskite Nanocrystals and Thin Films: Toward Efficient LEDs and Solar Cells. *Angew. Chem., Int. Ed.* **2021**, *60*, 21636.
(64) Byranvand, M. M.; Saliba, M. Defect Passivation of Perovskite Films for Highly Efficient and Stable Solar Cells. *Solar RRL* **2021**, *5* (8), 2100295.
(65) Jariwala, S.; Sun, H.; Adhyaksa, G. W. P.; Lof, A.; Muscarella, L. A.; Ehrler, B.; Garnett, E. C.; Ginger, D. S. Local Crystal Misorientation Influences Non-Radiative Recombination in Halide Perovskites. *Joule* **2019**, *3* (12), 3048−3060.
(66) Song, T. B.; Chen, Q.; Zhou, H.; Jiang, C.; Wang, H. H.; Yang, Y. M.; Liu, Y.; You, J.; Yang, Y. Perovskite Solar Cells: Film Formation and Properties. *Journal of Materials Chemistry A* **2015**, *3* (17), 9032−9050.
(67) Kato, M.; Fujiseki, T.; Miyadera, T.; Sugita, T.; Fujimoto, S.; Tamakoshi, M.; Chikamatsu, M.; Fujiwara, H. Universal Rules for Visible-Light Absorption in Hybrid Perovskite Materials. *J. Appl. Phys.* **2017**, *121* (11), 115501.
(68) Shirayama, M.; Kadowaki, H.; Miyadera, T.; Sugita, T.; Tamakoshi, M.; Kato, M.; Fujiseki, T.; Murata, D.; Hara, S.; Murakami, T. N.; Fujimoto, S.; Chikamatsu, M.; Fujiwara, H. Optical Transitions in Hybrid Perovskite Solar Cells: Ellipsometry, Density Functional Theory, and Quantum Efficiency Analyses for $CH_3NH_3PbI_3$. *Physical Review Applied* **2016**, *5* (1), 014012.